Supplementary Information (SI)

Reversible Hydration-Induced Ionic Conductivity Switching Accompanied by Large Desorption Enthalpy in Sodium Salts of 1,2,3-Triazole-Fused *p*-Benzoquinone

Shiori Harada,[a] Shun Dekura,*[ab] Genki Saito,[a] Tetsu Sato,[ab] and Tomoyuki Akutagawa*[ab]

[a] *Graduate School of Engineering, Tohoku University, Sendai 980-8579, Japan*

[b] *Institute of Multidisciplinary Research for Advanced Materials (IMRAM), Tohoku University, 2-1-1 Katahira, Aoba-ku, Sendai 980-8577, Japan*

E-mail s.dekura@tohoku.ac.jp, akutagawa@tohoku.ac.jp

Table of Contents

Experimental Section

Materials

The following reagents and solvents were purchased from commercial suppliers and used as received without purification: chloranil (Tokyo Chemical Industry Co., Ltd.), potassium phthalimide (Tokyo Chemical Industry Co., Ltd.), acetonitrile (Kanto Chemical Co.,Inc.), hydrazine monohydrate (FUJIFILM Wako Pure Chemical Corporation), sodium nitrite (FUJIFILM Wako Pure Chemical Corporation), acetic acid (Nacalai Tesque, Inc.), hydrochloric acid (35.0–47.0%, FUJIFILM Wako Pure Chemical Corporation), ethanol (Nacalai Tesque, Inc.), sodium hydroxide (FUJIFILM Wako Pure Chemical Corporation).

Sample preparation

H_2BTBQ, **NaHBTBQ**·2H_2O, and **Na_2BTBQ**·4H_2O were synthesized following the previously reported method.[1] The synthesized molecules were characterized by elemental analysis supported by the Central Analytical Facility, Institute of Multidisciplinary Research for Advanced Materials, Tohoku University, Japan. Elemental analyses were performed on a Microcoder JM10 (J-Science Lab Co.,Ltd.).

Synthesis of 2,3,5,6-tetraamino-*p*-benzoquinone (1)

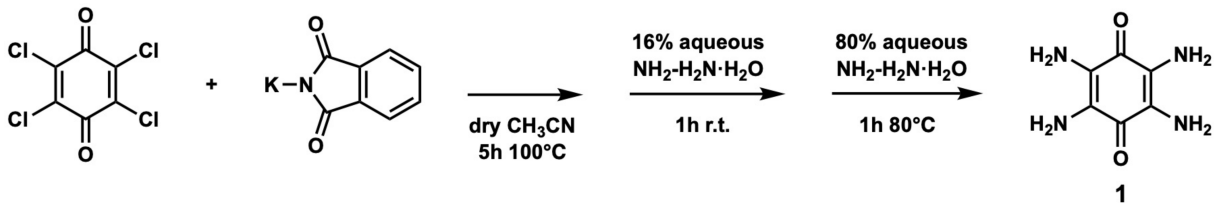

Chloranil (8.47 g, 0.0344 mol) and potassium phthalimide (25.0 g, 0.135 mol) were suspended in 193 mL of anhydrous acetonitrile, which was refluxed at 100 °C for 5 hours. After cooling it down to room temperature, the reaction suspension was collected by suction filtration, washed with water, dried under vacuum overnight to yield a green solid. A 16% aqueous solution of hydrazine monohydrate was slowly added dropwise to the green solid, and then the mixture was stirred for 1 hour with a mechanical stirrer. The reaction suspension was then collected by suction filtration and washed with water to yield a reddish-brown solid. An 80% aqueous solution of hydrazine monohydrate was slowly added dropwise to the reddish-brown solid, and the mixture was stirred at 80 °C for 1 hour. The hot reaction suspension was then immediately collected by suction filtration. The obtained solid was washed thoroughly with water, yielding the desired product **1** as a dark violet solid (2.65 g, 47.4% yield). Formula calc. for $C_6H_8N_4O_2$ (**1**): C,42.86; H,4.80; N,33.32. found: C,42.63; H,4.93; N,33.20.

Synthesis of NaHBTBQ

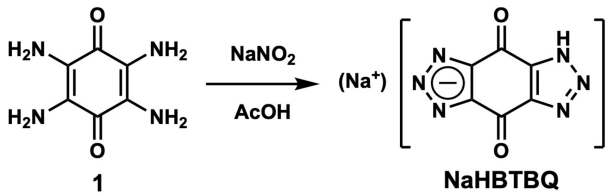

Acetic acid (160 mL) was added to **1** (3.36 g, 0.0200 mol) to form a suspension. Separately, sodium nitrite (4.44 g, 0.0643 mol) was dissolved in 80 mL of water to prepare an sodium nitrite aqueous solution, which was then slowly added dropwise to the suspension of **1** over 5 minutes. After stirring at room temperature for 24 hours, the reaction suspension was collected by suction filtration, and washed thoroughly with water to obtain a reddish-brown crude product. The crude product was recrystallized from water to yield **NaHBTBQ**·$2H_2O$ as yellow solid (1.0021 g, 18.4% yield). Formula calc. for $C_6H_5N_6O_4Na$ (**NaHBTBQ**·$2H_2O$): C,29.04; H,2.03; N,33.87. found: C,28.80; H,2.21; N,33.57.

Single crystals of **NaHBTBQ**·$2H_2O$ were grown by recrystallization from water/methanol mixed solvent (water:methanol = 9:1), yielding plate-like yellow crystals.

Synthesis of H_2BTBQ

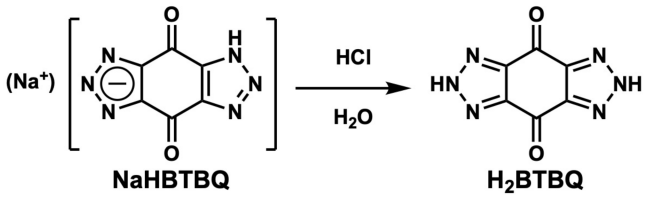

NaHBTBQ·$2H_2O$ (2.21 g, 0.00956 mol) was dissolved in 290 mL of hot water, where pH was then adjusted to 1 by the dropwise addition of hydrochloric acid. The solution was allowed to cool slowly to room temperature. The resultant precipitate was collected by suction filtration and washed with a small amount of ethanol to yield **H_2BTBQ** as a pale yellow solid (0.6857 g, 37.7% yield). Formula calc. for $C_6H_2N_6O_2$ (**H_2BTBQ**): C,37.91; H,1.06; N,44.20. found: C,37.61; H,1.23; N,44.03.

Single crystals of **H_2BTBQ** were grown by slow evaporation of methanol solution, yielding plate-like pale yellow crystals.

Synthesis of Na_2BTBQ

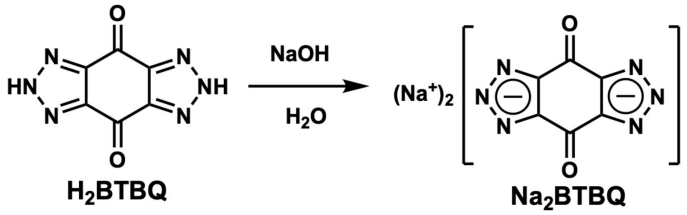

H_2BTBQ (0.963 g, 0.00507 mol) was dissolved in 290 mL of hot water, to which 13 mL of 1 M sodium hydroxide aqueous solution was added. The solution was allowed to cool slowly to room temperature. The resultant precipitate was collected by suction filtration and washed with

water to yield **Na_2BTBQ**·4H_2O as yellow solids (0.591 g, 38.1% yield). Formula calc. for $C_6H_8N_6O_6Na_2$ (**Na_2BTBQ**·4H_2O): C,23.54; H,2.63; N,27.54. found: C,23.67; H,2.66; N,27.39. Single crystals of **Na_2BTBQ**·4H_2O were grown by recrystallization from water, yielding needle-like dark yellow crystals.

Thermal analysis

Thermogravimetric (TG) analysis was conducted using a Thermo plus TG8121 thermal analysis station (Rigaku Corp.) with an Al_2O_3 reference and rate of 10 K min^{-1} under nitrogen gas flow. Powder samples or small crystals were collected for the measurements. Differential scanning calorimetry (DSC) was performed using DSC3 STARe Sytem (METTLER TOLEDO) with an Al reference and rate of 5 K min^{-1} under nitrogen gas flow. Powder samples ground using mortar and pestle were used for the measurements.

Single-crystal X-ray structural analysis

Crystallographic data were collected using a RAPID-II diffractometer (Rigaku Corp.) equipped with a rotating anode fitted with multilayer confocal optics and Cu $K\alpha$ (λ = 1.54187 Å) radiation from a graphite monochromator and the nitrogen gas blowing temperature controller. Using Olex2-1.5 (OlexSys),[2] the structure was solved with the SHELXT (version 2014/5)[3] structure solution program using Intrinsic Phasing and refined with the SHELXL (version

2018/3)[4] refinement package using Least Squares minimization. Anisotropic thermal parameters were applied to non-hydrogen atoms.

Powder X-ray diffraction (PXRD)

PXRD patterns of **H_2BTBQ**, **NaHBTBQ**·2H_2O, **Na_2BTBQ**·4H_2O at 100 K were measured by using a RAPID-II diffractometer (Rigaku Corp.) equipped with a rotating anode fitted with multilayer confocal optics and Cu $K\alpha$ (λ = 1.54187 Å) radiation from a graphite monochromator and the nitrogen gas blowing temperature controller. Variable-temperature(VT)-PXRD of **NaHBTBQ**·$x$$H_2O$ (x = 0, 2) and **Na_2BTBQ**·$y$$H_2O$ (y = 0, 2, 4) as well as their re-hydrated samples were performed by using a Smart Lab 3kW diffractometer (Rigaku Corp.) with Cu K_a radiation at λ = 1.54187 Å and a custom-made temperature controller.

Water sorption isotherms

Adsorption isotherms water vapor were measured using BELSORP-maxII (MicrotracBEL) at 298 K. The water used for the measurements were subjected to three degassing treatments before measurement to remove dissolved gases, and each sample was vacuum dried at 453 K for 12 hours before measurements.

Alternating current (AC) impedance spectroscopy

Temperature(*T*)- and frequency(*f*)-dependent dielectric constants were measured using the quasi-four-probe AC impedance method from 100 Hz to 1 MHz with a HP4194A impedance/gain-phase analyzer (Hewlett-Packard) and a LTS-420E temperature controller (Linkam Scientific Instruments). The polycrystalline powder samples were ground and fabricated as 3 mmφ compressed pellets, on the both side of which the electrodes were made using Ag paste (DuPont 4922N) and 25 μmφ gold wires for dielectric measurements. For the hydrated samples, the pellets were coated with CYTOP CTX-809SP2 (AGC Chemicals Company), which were then covered with a heat-resistant epoxy resin 2088E (ThreeBond) to prevent water desorption.

The ionic conductivities, σ, were estimated by fitting analyses to the complex impedance *Z** using an equivalent circuit (Fig. S1), which correspond to the fitting function shown below;

$$Z^* = Z_1 - iZ_2 = R_\mathrm{c} + \frac{R_\mathrm{s}}{1 + (i2\pi f R_\mathrm{s} C_\mathrm{s})^\alpha},$$

where Z_1 and Z_2 are the real and imaginary parts of the complex impedance Z^*, R_c is contact resistance, R_s is sample resistance, C_s is sample capacitance, and α is exponent factor ($0 < \alpha \leq 1$).

Because the sample colors were light, we ruled out the possibility of electronic conduction, and attributed the dielectric relaxation to ionic conduction. We attributed the ionic conduction to

protonic conduction, not to sodium ion conduction, because the anhydrous samples did not show any dielectric responses and there is no plausible conduction pathway for sodium ions in the crystal structures whereas the extended hydrogen-bond networks exist in the structures.

The activation energies E_a for the proton conductivities were estimated by the Arrhenius equation:

$$\sigma T = \sigma_0 \exp\left(-\frac{E_a}{k_B T}\right),$$

where σ_0 is a prefactor, k_B is the Boltzmann's constant.

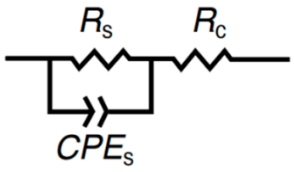

Fig. S1. The equivalent circuit used for fitting analyses (R_s: sample resistance, R_c: contact resistance, CPE_s: constant-phase element for the sample).

Density functional theory (DFT) calculations

Relative stability of crystal water molecules in **Na_2BTBQ**·4H_2O were evaluated by using DFT calculations. The calculations were performed using OpenMX software (Ver. 3.9.9-1) based on optimized localized basis functions and pseudopotentials (PPs). The basis functions used were H6.0-s2p1, C6.0-s2p2d1, N6.0-s2p2d1, O6.0-s2p2d1, and Na9.0-s3p2d1 for hydrogen, carbon,

nitrogen, oxygen, and sodium, respectively; in the abbreviation of basis functions such as C6.0-s2p2d1, C is the atomic symbol, 6.0 represents the cutoff radius (bohr) in the generation by the confinement scheme, and s2p2d1 indicates the employment of two, two, and one optimized radial functions for the s-, p-, and d-orbitals, respectively. The radial functions were optimized by a variational optimization method.[5,6] As valence electrons in the PPs, we included 1s for hydrogen; 2s and 2p for carbon, nitrogen and oxygen; 2s, 2p, and 3s for sodium. All the PPs and pseudo-atomic orbitals used in this study were taken from the database (2019) on the OpenMX website, which was benchmarked by the delta gauge method.[7] Real space grid techniques were used for the numerical integrations and the solution of the Poisson equation using fast Fourier transform with an energy cutoff of 300 Ryd.[8] We used a generalized gradient approximation (GGA) proposed by Perdew, Burke, and Ernzerhof to the exchange–correlation functional.[9] An electronic temperature of 300 K was used to count the number of electrons by the Fermi–Dirac function for all the systems considered. For k-point sampling, we used a regular mesh of 1 × 1 × 2. Grimme's DFT-D3 dispersion correction was applied to take into account van der Waals interactions.[10,11]

For the initial state of **Na_2BTBQ**·4H_2O, single-crystal structure was used and only hydrogen atoms were geometrically optimized. The optimized **Na_2BTBQ**·4H_2O structure was divided into two parts: the guest 2H_2O part (= 2H_2O⊂**Na_2BTBQ**·4H_2O) and the host **Na_2BTBQ**·2H_2O part (= **Na_2BTBQ**·4H_2O−2H_2O). The interaction energies of the guest 2H_2O with the host

Na₂BTBQ·2H_2O were evaluated by using the total energies of the optimized **Na₂BTBQ**·4H_2O, the guest 2H_2O ⊂ **Na₂BTBQ**·4H_2O, and the host **Na₂BTBQ**·4H_2O−2H_2O structures, where basis set superposition errors (BSSEs) were corrected based on counterpoise method.

$$\Delta E = E(\mathbf{Na_2BTBQ} \cdot 4H_2O) - \{E(\mathbf{Na_2BTBQ} \cdot 4H_2O - 2H_2O) + E(2H_2O \subset \mathbf{Na_2BTBQ} \cdot 4H_2O)\}$$

The calculated ΔE values are quite low (ΔE < −400 kJ (mol-H_2O)$^{-1}$). This is because the hypothetical structures of the host **Na₂BTBQ**·4H_2O−2H_2O are not the optimized stable structures for **Na₂BTBQ**·2H_2O and possess drastically different molecular arrangements from the actual structure of **Na₂BTBQ**·2H_2O (Fig. S10). Still, the relative interaction energies and the stability trend can be discussed.

Results and Discussion

Single-crystal structures

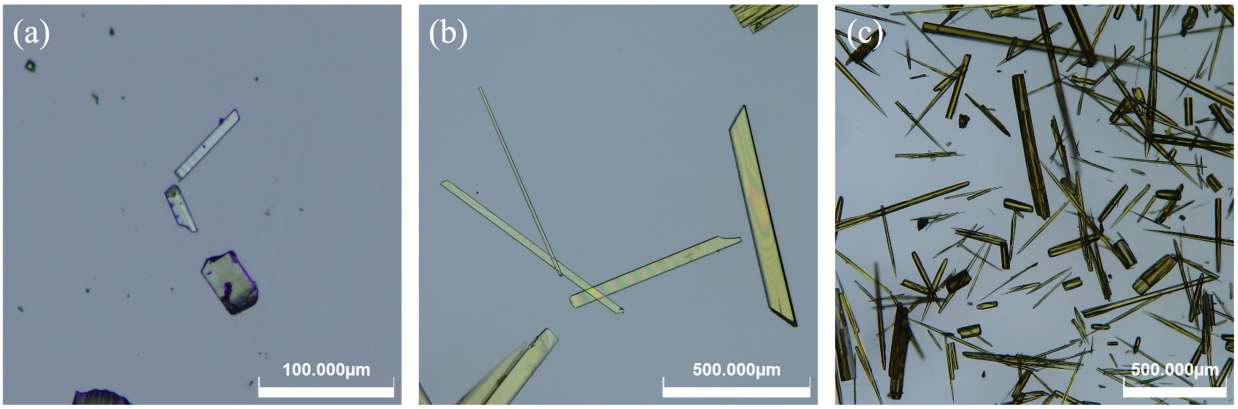

Fig. S2. Optical microscope images of (a) **H_2BTBQ**, (b) **NaHBTBQ**·2H_2O, and (c) **Na_2BTBQ**·4H_2O.

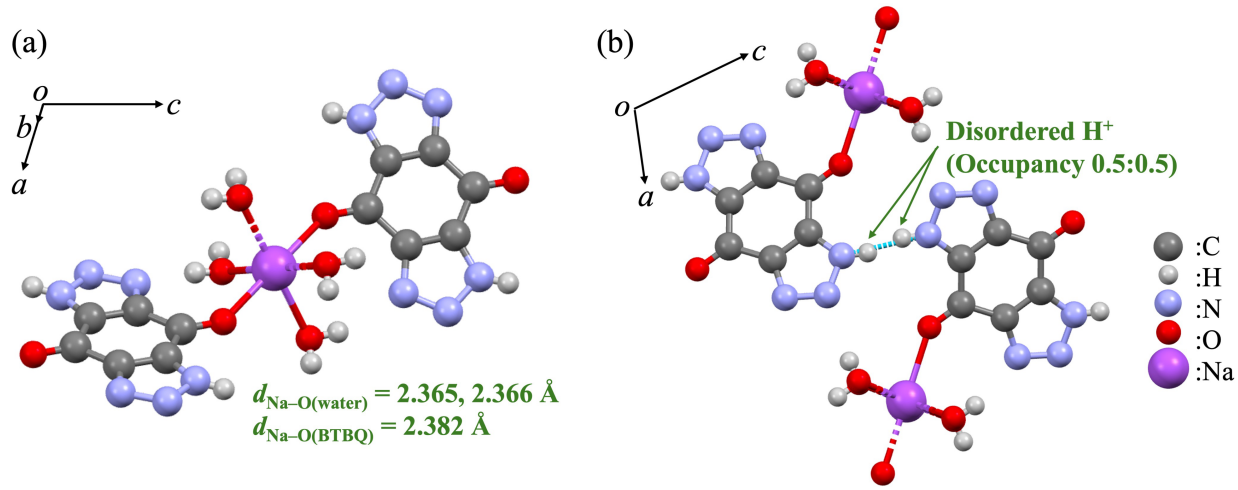

Fig. S3. The local structures of **NaHBTBQ**·2H_2O around (a) Na^+ cation and (b) N···H···N hydrogen bond at 100 K.

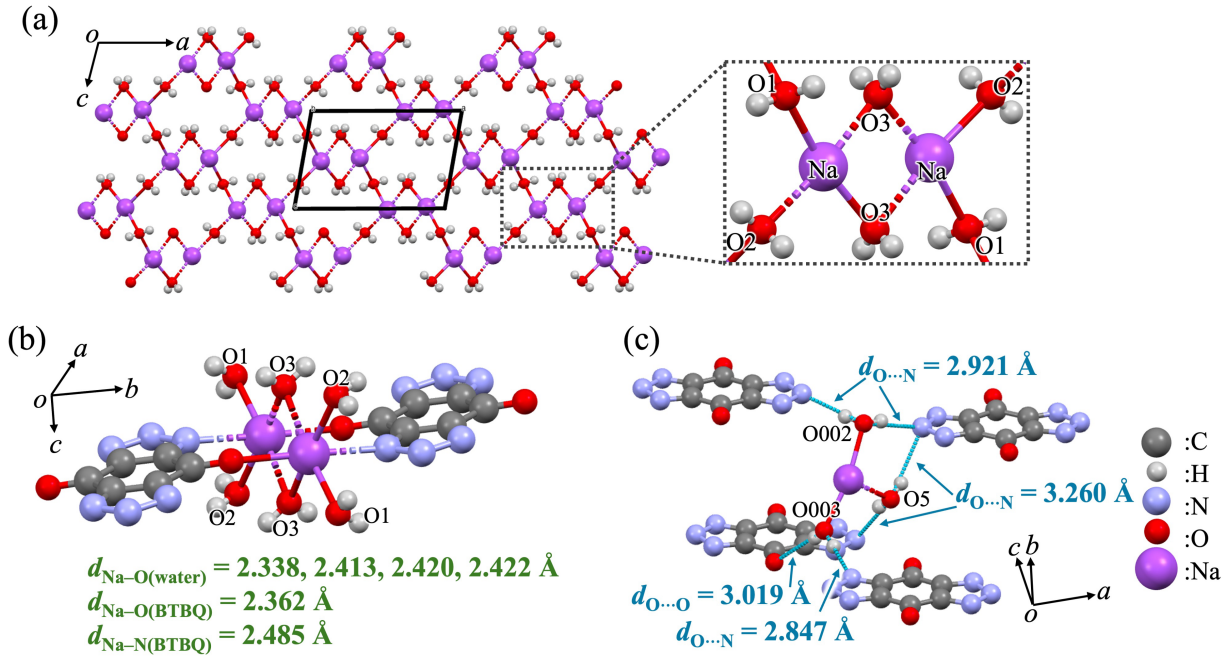

Fig. S4. Crystal structure of **Na_2BTBQ**·4H_2O at 100 K.

Table S1. Crystallographic parameters.

Crystal	**H_2BTBQ** (This time)	**H_2BTBQ** (reported)[1]	**NaHBTBQ**·2H_2O (This time)	**NaHBTBQ**·2H_2O (reported)[1]
Chemical formula	$C_6H_2N_6O_2$	$C_6H_2N_6O_2$	$C_6H_4N_6NaO_4$	$C_6H_4N_6NaO_4$
Formula weight	190.14	190.12	247.14	247.13
T / K	100	100	100	100
Crystal system	*Monoclinic*	*Monoclinic*	*Monoclinic*	*Monoclinic*
Space group	$P2_1/c$	$P2_1/c$	$P2/n$	$P2/n$
a /Å	6.4630(5)	6.46087(12)	9.6887(8)	9.6805(2)
b / Å	5.6431(4)	5.62884(12)	3.5289(3)	3.52584(8)
c / Å	9.3752(7)	9.37402(17)	14.4250(13)	14.4065(3)
α / °	90	90	90	90
β / °	99.209(7)	99.3001(9)	106.833(7)	106.8049(13)
γ / °	90	90	90	90
V / Å^3	337.52(3)	336.426(11)	472.07	470.718(17)
Z	2	2	2	2
ρ_{calc} / g·cm^{-3}	1.871	1.877	1.739	1.743
μ / cm^{-1}	1.296	1.302	1.668	1.672
Radiation	Cu K_α	Cu K_α	Cu K_α	Cu K_α
Reflections collected/unique	2680/613	3334/618	3531/839	4412/861
R_{int}	0.0816	0.0580	0.0538	0.0805
R_1 [$I >= 2\sigma(I)$][a]	0.0371	0.0421	0.0641	0.0577
wR_2 [all data][a]	0.0991	0.1103	0.1718	0.1700
GOF	1.085	1.087	1.073	1.085

Na_2BTBQ·4H_2O (This time)	**Na_2BTBQ**·4H_2O (reported)[12]
$C_6H_8N_6Na_2O_6$	$C_6H_8N_6Na_2O_6$
306.16	306.16
100	293(2)
Monoclinic	Monoclinic
*C*2/*c*	*C*2/*c*
10.4251(7)	10.4329(7)
15.5308(10)	15.5499(10)
6.8569(5)	6.8575(4)
90	90
100.180(7)	100.221(2)
90	90
1092.72(13)	1094.84(12)
4	4
1.861	1.857
2.082	2.26
Cu K_α	Mo K_α
6026/990	12452/1367
0.0943	0.0557
0.0540	0.0346
0.1509	0.0841
1.111	1.070

[a] $R_1 = \Sigma||F_o| - |F_c|| / \Sigma |F_o|$ and $wR_2 = (\Sigma\omega(|F_o| - |F_c|)^2 / \Sigma\omega F_o^2)^{1/2}$.

PXRD patterns

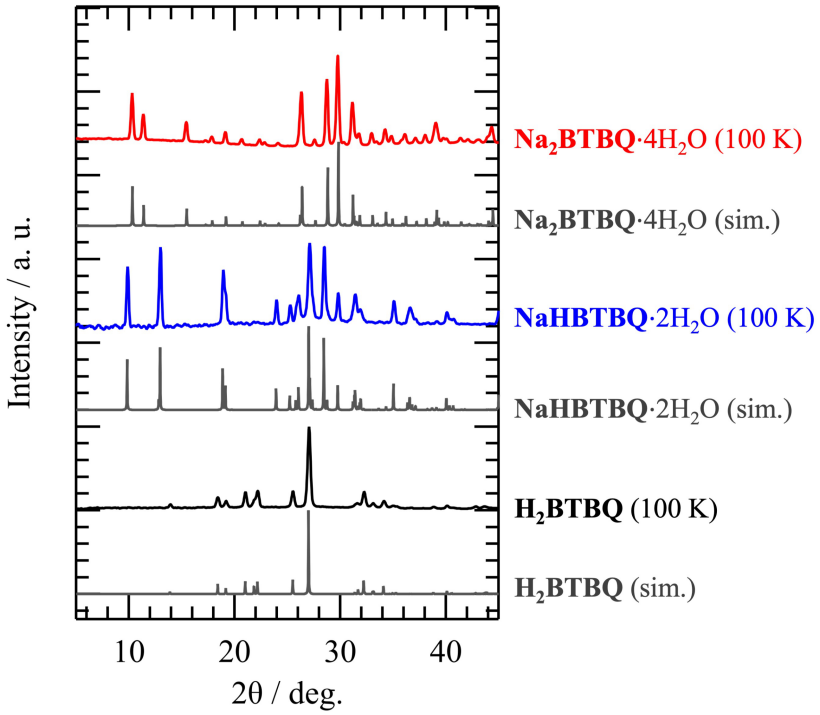

Fig. S5. PXRD patterns of the powder samples of **H_2BTBQ**, **NaHBTBQ**·$2H_2O$, and **Na_2BTBQ**·$4H_2O$ measured at 100 K, compared with the simulation patterns based on the single-crystal structures.

Thermal analysis

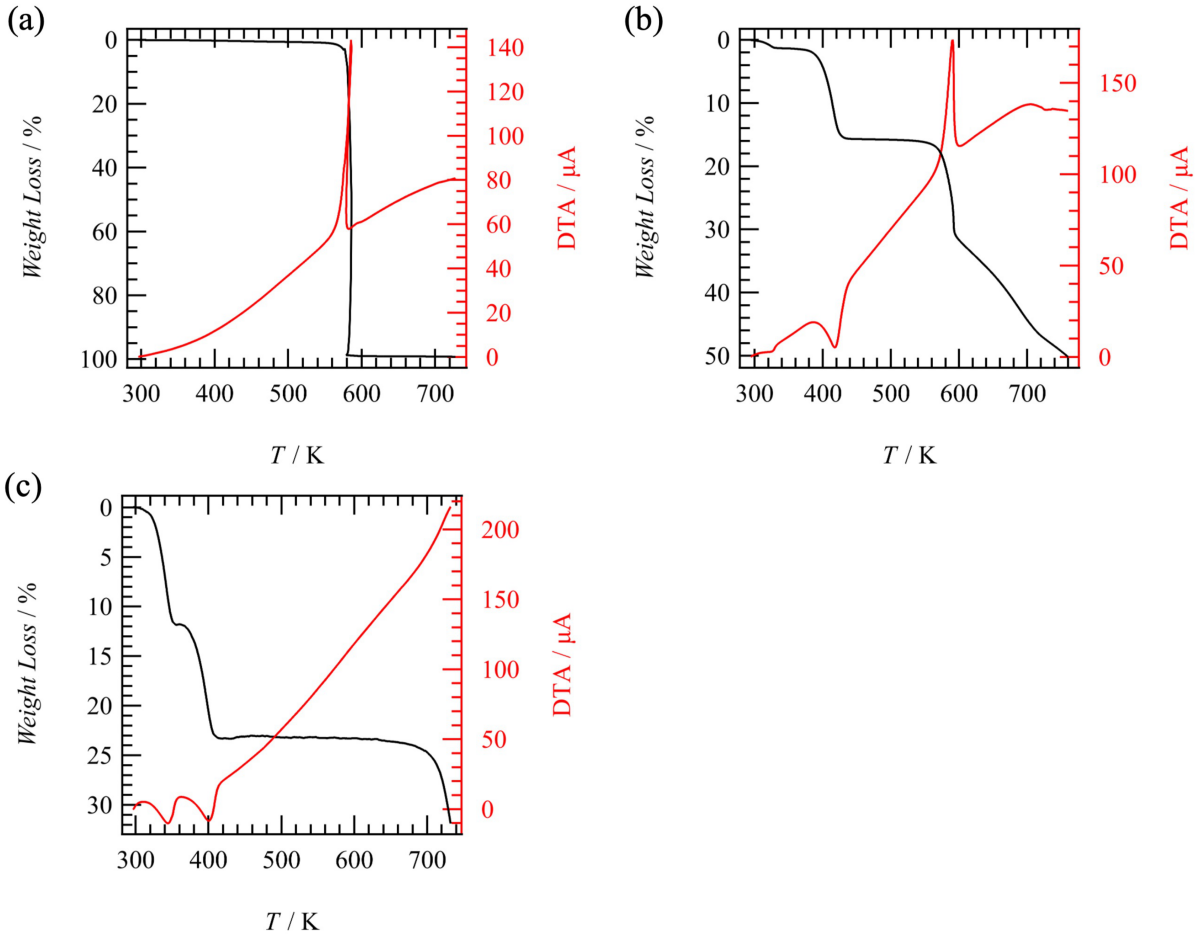

Fig. S6. TG-DTA charts for (a) **H_2BTBQ**, (b) **NaHBTBQ**·2H_2O, and (c) **Na_2BTBQ**·4H_2O.

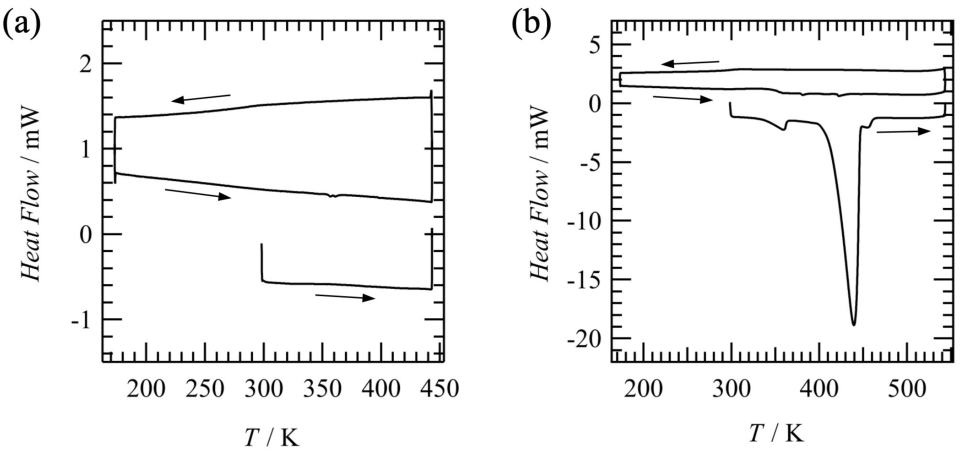

Fig. S7. DSC charts of (a) **H_2BTBQ** and (b) **NaHBTBQ**·2H_2O.

Table S2. Water desorption enthalpies and the desorption temperatures of **NaHBTBQ**·2H_2O and **Na_2BTBQ**·4H_2O compared with the typical reported solid sorbents for water adsorption cooling.

Material	ΔH / kJ (mol-H_2O)$^{-1}$	ΔH / kJ $g^{-1}_{adsorbent}$	Desorption temperature / K
Water[13]	40.65 (373 K)	2.256	373
Silica gel[14]	45.2–48.8	1.08–1.13	ca. 330–360
$MgCl_2$·6H_2O[15]	50.9 (to $MgCl_2$·2H_2O)	1.55	ca. 390
$CaCl_2$·4H_2O[15]	52.8	1.90	ca. 420
MOF-801[16]	53.3	0.592	ca. 380
Zeolite MgY[16]	71.8	1.43	ca. 670
Calcium ceftriaxone heptahydrate[17]	61.1	0.722	ca. 420
Calcium L-lactate pentahydrate[18]	50.0	1.15	ca. 390
NaHBTBQ·2H_2O (This work)	**60.20**	**0.5676**	**438**[a]
Na_2BTBQ·4H_2O (This work)	**50.45 (Step 1)** **57.05 (Step 2)**	**0.3735** **0.4874**	**373 (Step 1)**[a] **433 (Step 2)**[a]

[a] The values were taken from the DSC peak top values.

Reversible water sorption behaviors

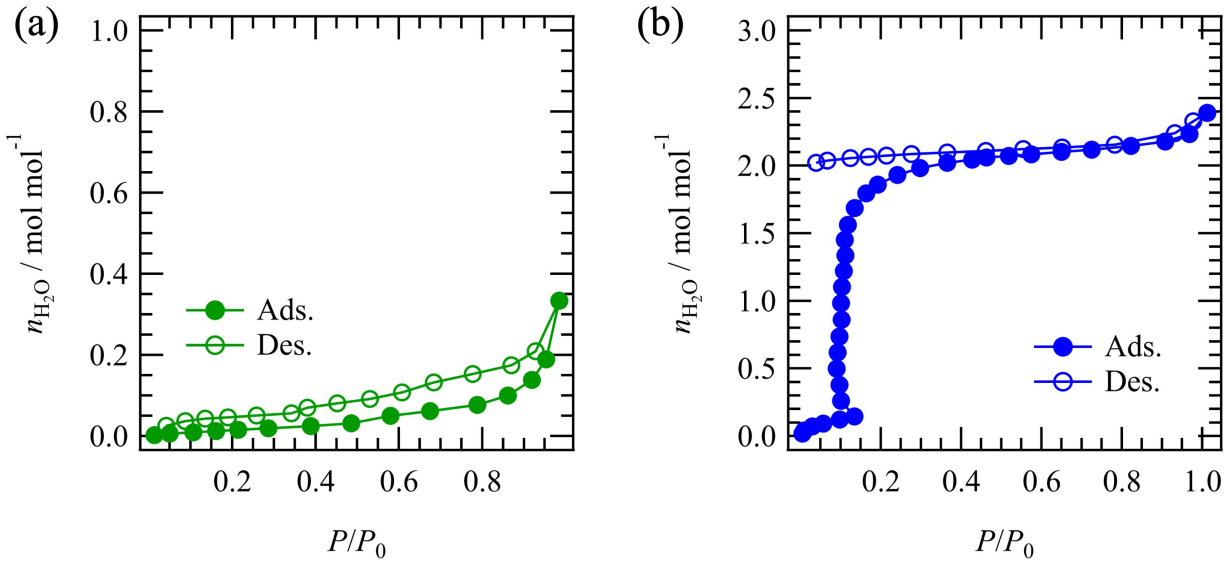

Fig. S8. Water vapor sorption isotherms of (a) **H_2BTBQ** and (b) **NaHBTBQ** at 298 K.

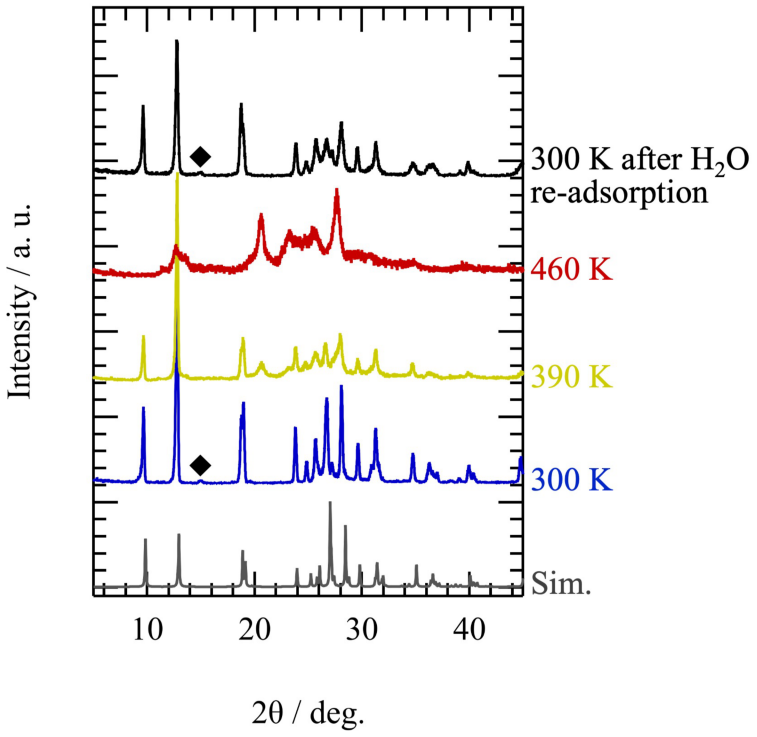

Fig. S9. Variable-temperature PXRD patterns of **NaHBTBQ**·2H_2O during water desorption followed by water re-adsorption. Filled diamonds at 2θ ~ 15° indicate unidentified peaks not matched with the simulation pattern of **NaHBTBQ**·2H_2O.

2-step water desorption in Na2BTBQ·4H$_2$O

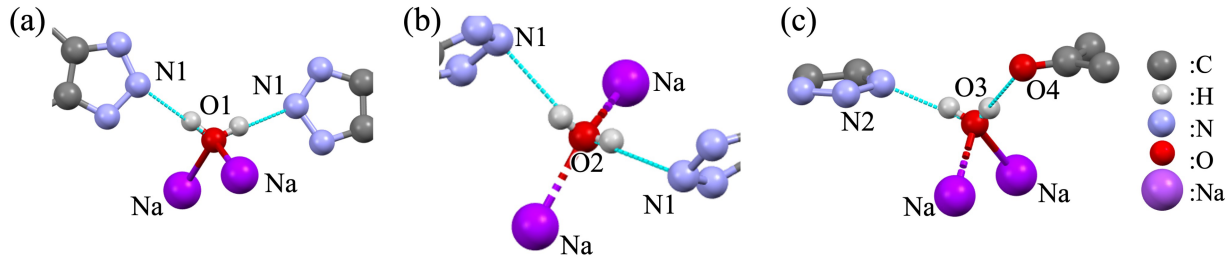

Fig. S10. The local structures around the water molecules with the atomic labels of (a) O1, (b) O2, and (c) O3 in **Na$_2$BTBQ**·4H$_2$O crystal.

Table S3. Interatomic distances around the water molecules with the atomic labels of O1, O2, and O3 in **Na$_2$BTBQ**·4H$_2$O crystal.

	O1	**O2**	**O3**
$d_{O–Na}$ / Å	2.413	2.442	2.338, 2.420
$d_{O\cdots N}$ / Å	2.921	3.260	2.847
$d_{O\cdots O}$ / Å	–	–	3.019

Table S4. The calculated total energies (per formula) of the optimized **2**·3Bz, the guest 2H$_2$O⊂**Na$_2$BTBQ**·4H$_2$O, and the host **Na$_2$BTBQ**·4H$_2$O−2H$_2$O structures.

	O1, O2	**O3**
E(**Na$_2$BTBQ**·4H$_2$O) / kJ mol^{-1}	−3078320.411	−3078320.411
E(**Na$_2$BTBQ**·4H$_2$O−2H$_2$O) / kJ mol^{-1}	−2710421.201	−2710379.278
E(2H$_2$O ⊂ **Na$_2$BTBQ**·4H$_2$O) / kJ mol^{-1}	−366949.523	−366995.049
ΔE / kJ (mol-H$_2$O)$^{-1}$	−474.844	−473.042
$\Delta E-\Delta E$(O3) / kJ (mol-H$_2$O)$^{-1}$	−1.802	0

Dielectric responses and ionic conductivities

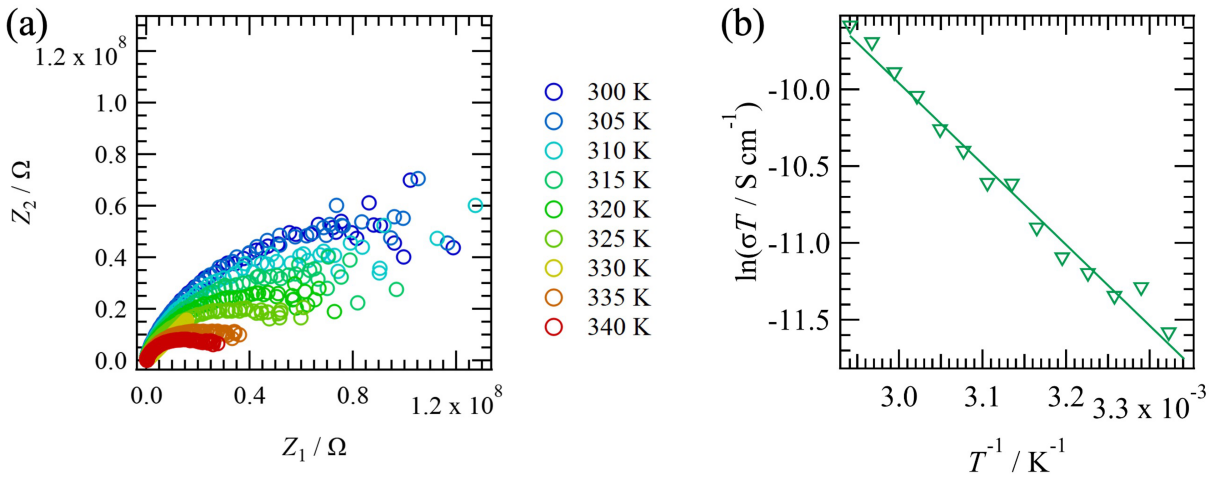

Fig. S11. (a) Nyquist plots for the complex impedance of **Na_2BTBQ**·2H_2O at various temperatures. (b) Arrhenius plot of the ionic conductivity for **Na_2BTBQ**·2H_2O. The solid line in (b) indicates the best fit using the Arrhenius equation.

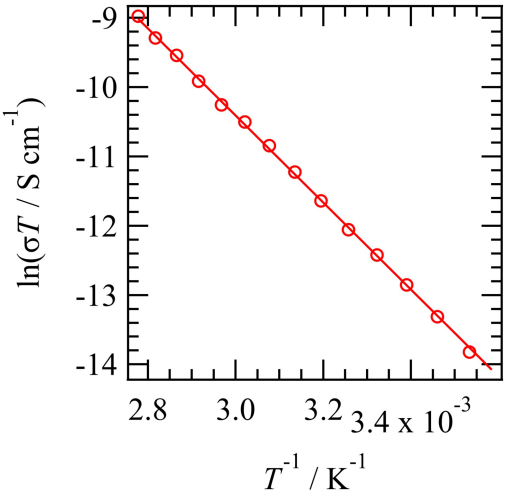

Fig. S12. Arrhenius plot of the ionic conductivity for **Na_2BTBQ**·4H_2O. The solid line indicates the best fit using the Arrhenius equation.

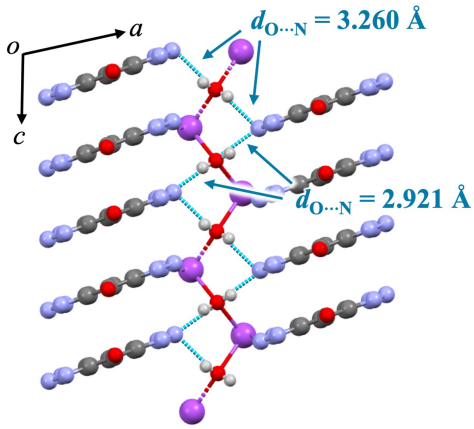

Fig. S13. The possible proton conduction pathway along the *c*-axis in **Na_2BTBQ**·4H_2O.

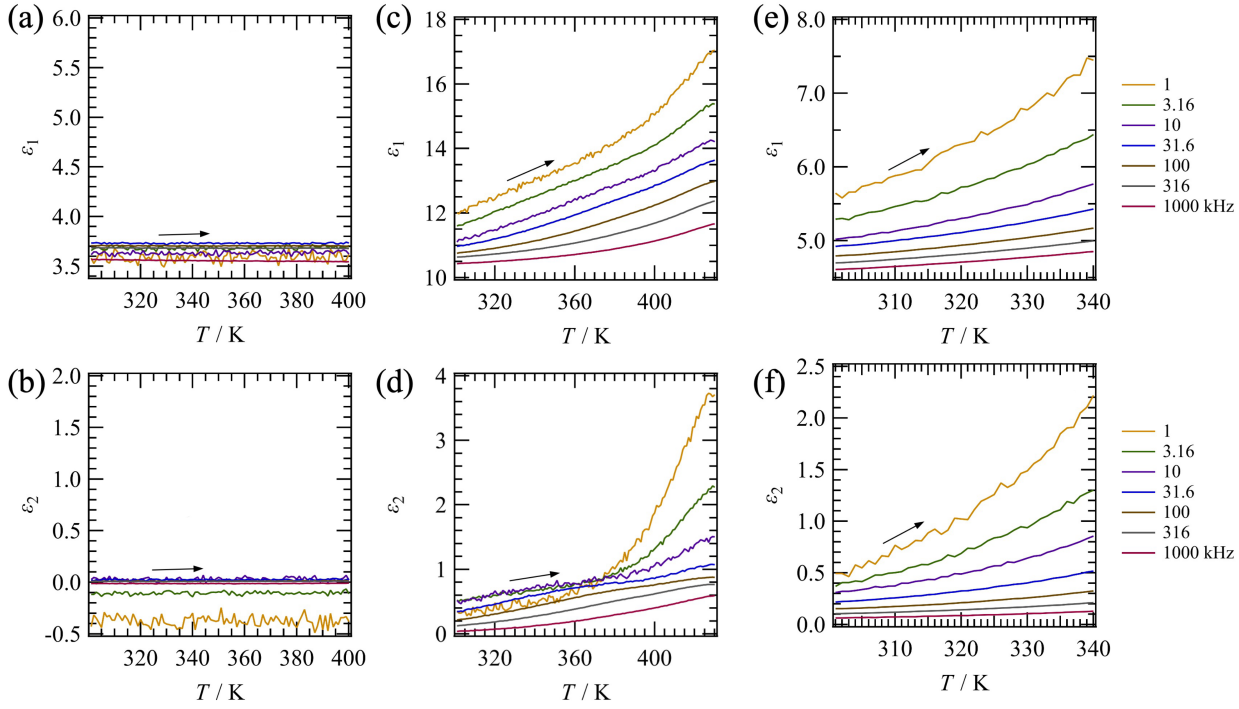

Fig. S14. Temperature(*T*)- and frequency(*f*)-dependent (a),(c),(e) real (ε_1) and (b),(d),(f) imaginary (ε_2) parts of the dielectric constants of (a),(b) **H_2BTBQ**, (c),(d) **NaHBTBQ**·0H_2O, and (e),(f) **NaHBTBQ**·2H_2O on heating processes.

References

1 M. Sato, T. Takeda, N. Hoshino and T. Akutagawa, *CrystEngComm*, 2017, **19**, 910–917.

2 O. V. Dolomanov, L. J. Bourhis, R. J. Gildea, J. A. K. Howard and H. Puschmann, *J. Appl. Crystallogr.*, 2009, **42**, 339–341.

3 G. M. Sheldrick, *Acta Crystallogr. B*, 2015, **71**, 3–8.

4 G. M. Sheldrick, *Acta Crystallogr. A*, 2015, **71**, 3–8.

5 T. Ozaki, *Phys. Rev. B.*, 2003, **67**, 155108.

6 T. Ozaki and H. Kino, *Phys. Rev. B.*, 2004, **69**, 195113.

7 K. Lejaeghere, G. Bihlmayer, T. Bjorkman, P. Blaha, S. Blugel, V. Blum, D. Caliste, I. E. Castelli, S. J. Clark, A. Dal Corso, S. de Gironcoli, T. Deutsch, J. K. Dewhurst, I. Di Marco, C. Draxl, M. Du ak, O. Eriksson, J. A. Flores-Livas, K. F. Garrity, L. Genovese, P. Giannozzi, M. Giantomassi, S. Goedecker, X. Gonze, O. Granas, E. K. U. Gross, A. Gulans, F. Gygi, D. R. Hamann, P. J. Hasnip, N. A. W. Holzwarth, D. Iu an, D. B. Jochym, F. Jollet, D. Jones, G. Kresse, K. Koepernik, E. Kucukbenli, Y. O. Kvashnin, I. L. M. Locht, S. Lubeck, M. Marsman, N. Marzari, U. Nitzsche, L. Nordstrom, T. Ozaki, L. Paulatto, C. J. Pickard, W. Poelmans, M. I. J. Probert, K. Refson, M. Richter, G.-M. Rignanese, S. Saha, M. Scheffler, M. Schlipf, K. Schwarz, S. Sharma, F. Tavazza, P. Thunstrom, A. Tkatchenko, M. Torrent, D. Vanderbilt, M. J. van Setten, V. Van Speybroeck, J. M. Wills, J. R. Yates, G.-X. Zhang and S. Cottenier, *Science*, 2016, **351**, aad3000–aad3000.

8 T. Ozaki and H. Kino, *Phys. Rev. B.*, 2005, **72**, 045121.

9 J. P. Perdew, K. Burke and M. Ernzerhof, *Phys. Rev. Lett.*, 1996, **77**, 3865–3868.

10 S. Grimme, J. Antony, S. Ehrlich and H. Krieg, *J. Chem. Phys.*, 2010, **132**, 154104.

11 S. Grimme, S. Ehrlich and L. Goerigk, *J. Comput. Chem.*, 2011, **32**, 1456–1465.

12 H. Bunzen, A. Lamp, M. Grzywa, C. Barkschat and D. Volkmer, *Dalton Trans.*, 2017, **46**, 12537–12543.

13 D. A. McQuarrie and J. D. Simon, *Physical Chemistry: A Molecular Approach*, University Science Books, Sausalito, CA, 1997.

14 H. T. Chua, K. C. Ng, A. Chakraborty, N. M. Oo and M. A. Othman, *J. Chem. Eng. Data*, 2002, **47**, 1177–1181.

15 H. U. Rammelberg, T. Schmidt and W. Ruck, *Energy Procedia*, 2012, **30**, 362–369.

16 H. Kim, H. J. Cho, S. Narayanan, S. Yang, H. Furukawa, S. Schiffres, X. Li, Y.-B. Zhang, J. Jiang, O. M. Yaghi and E. N. Wang, *Sci. Rep.*, 2016, **6**, 19097.

17 E. Mastronardo, E. La Mazza, D. Palamara, E. Piperopoulos, D. Iannazzo, E. Proverbio and C. Milone, *Energies*, 2022, **15**, 4339.

18 J.-B. De Maere D'aertrycke, J. Morlot, K. Robeyns, Y. Filinchuk and T. Leyssens, *Food Chem.*, 2020, **325**, 126884.